Catalysis Science & Technology

Accepted Manuscript

ROYAL SOCIETY OF CHEMISTRY

www.rsc.org/catalysis

The performance and mechanism of Ag-doped CeO_2 /TiO_2 catalyst on the catalytic oxidation of gaseous elemental mercury

Songjian Zhao, Zan Qu, Naiqiang Yan*, Zhen Li, Haomiao Xu, Jian Mei, Fuquan Quan

School of Environmental Science and Engineering, Shanghai Jiao Tong University, 800 Dong Chuan Road, Shanghai, 200240, PR China. E-mail addresses: nqyan@sjtu.edu.cn Fax: +86 21 54745591; Tel: +86 21 54745591

Abstract

To improve the catalytic oxidation ability of the CeO_2/TiO_2 catalyst for gaseous elemental mercury, silver was introduced. Doping with Ag can significantly enhance the Hg^0 oxidation ability of CeO_2/TiO_2. In addition, the temperature window was wide (from 150 to 450 ℃). The catalysts were characterized by TEM, XRD, XPS and H_2-TPR. The results indicated that silver nanoparticles can be loaded by the support of TiO_2. The catalysts had better crystallization and the higher redox ability after adding silver. The silver existed mostly in its metallic state, which can keep Ce in a higher Ce (IV) state, and HCl was oxidized into active Cl by CeO_2 and then was adsorbed on the silver nanoparticles. In addition to the HCl and Hg^0 breakthrough experiments, a Hg^0 desorption experiment and Cl_2 yield experiment were conducted to study the catalytic mechanisms of the elemental mercury oxidation at various temperature ranges; these experiments indicated that the reaction was followed by the Langmuir Hinshelwood mechanism at a low temperature, and by the Eley Rideal mechanism and the homogeneous gas-phase reaction at high temperature. Furthermore, a mercury valence state change experiment was analyzed to indicate that HCl was the major catalytic oxidization component.

1. Introduction

Elemental mercury emitted into atmosphere during the process of coal combustion will pollute the air and cause adverse effects to the health of humans.[1] Therefore, many measures have been taken to reduce mercury emissions in recent decades. The U.S. EPA updated the emission limits for new power plants under the Mercury and Air Toxics Standards (MATS) on March 28, 2013.[2] In October 2013, a new international convention to control mercury emissions named the Minamata Convention on Mercury was signed by most countries, which was a response to the issue of the global mercury pollution problem.[3]

Mercury exists in three forms in coal-fired flue gas: elemental mercury (Hg^0), oxidized mercury (Hg^{2+}) and particulate-bound mercury (Hg^p). Hg^{2+} and Hg^p are relatively easy to remove from flue gas by typical air pollution control devices. However, elemental mercury (Hg^0) is difficult to remove from flue gas due to its high equilibrium volatility and low solubility in water.[4] Therefore, it is necessary to develop effective technologies to remove Hg^0. The catalytic conversion of Hg^0 to its oxidized form by catalysts subsequently captured by existing air pollution control devices is considered to be an effective method for Hg^0 control.

In recent years, a great deal of research into metal oxide catalysts has been extensively conducted to develop effective Hg^0 oxidation technologies.[5-8] CeO_2 was heralded due to its large oxygen storage capacity and unique redox couple Ce^{3+}/Ce^{4+} with the ability to shift between CeO_2 and Ce_2O_3 under oxidizing and reducing conditions, respectively, which was used for the catalytic oxidation of elemental

mercury.[9, 10] However, the appropriate temperature window of Hg^0 oxidation was not wide, and the efficiency of Hg^0 oxidation over CeO_2-TiO_2 catalysts depends on the HCl concentration of the flue gas.[11]

Silver has long been recognized as an effective catalytic component and has been shown to facilitate the redox process. [12, 13] Delaigle et al. used V_2O_5/TiO_2 catalysts which added silver in the oxidation of chlorobenzene, which maintained the vanadium in a higher oxidation state and induced higher catalytic performances.[14] Ma et al. prepared Ag/CeO_2 nanosphere catalysts for formaldehyde oxidation and found that synergetic interactions might exist between the Ag and CeO_2 nanosphere, and the presence of silver could facilitate surface chemisorbed oxygen activation, which mainly contributed to the HCHO oxidation.[15] In addition, silver has been recognized as an efficient adsorbent for the capture of Hg^0 at low temperatures through an amalgamation mechanism. Thus, the combination of Ag and Ce may be feasible, which can enhance the Hg^0 catalytic efficiency and widen the temperature window of the reaction.

In the present study, catalysts were prepared using a room-temperature impregnation method. The physical and chemical properties of the catalysts, as well as the Hg^0 oxidation efficiency, were investigated. Furthermore, the catalytic mechanisms involved in improving the efficiency at various temperatures were discussed.

2. Experimental section

2.1 Materials.

Commercially available TiO_2 powder (Degussa P25) was mainly used as the carrier of various catalysts, which was a standard material for all purposes and contained anatase and rutile phases in a ratio of approximately 3:1. All chemicals used for the catalysts' preparation were of analytical grades and were purchased from Sigma-Aldrich Co. and Sino-pharm Chemical Reagent Co. The standardized SO_2 (10000 ppm), NO (5000 ppm) and HCl (2000 ppm and 5%) gases were provided by Dalian Date Gas Co.

2.2 Preparation of Catalysts.

Catalysts were prepared by the impregnation method, which included CeO_2-TiO_2, Ag-TiO_2 and Ag-CeO_2-TiO_2. An appropriate amount of P25 was added to the $(NH_4)_2Ce(NO_3)_6$ solution and stirred for 1 h, which was marked as the "A" solution. The polyvinylpyrrolidone (PVP) was dissolved in water, and the $AgNO_3$ precursor was then added. The mixed solution was stirred for 6 h at room temperature and was marked as the "B" solution. The B solution was added dropwise into the A solution and stirred constantly for 2 h. The mixed solution was then evaporated and dried with the rotary evaporation apparatus and was then finally calcined in a muffle furnace (5 h, 500 ℃). The CeO_2-TiO_2, Ag-TiO_2 and Ag-CeO_2-TiO_2 catalysts were labeled as Ce-Ti, Ag-Ti and Ag-Ce-Ti. The proportion of the Ce and Ag to TiO_2 is on the basis of the atom percentages, such that Ce(x%)-Ti represents the CeO_2/TiO_2 mole ratio, and 1% was omitted.

2.3 Catalytic Activity Evaluation.

The catalytic activity was evaluated in a simulated gas preparation system and a catalytic reaction device, in which a cold vapor atomic absorption spectrometer (CVAAS) and an online data acquisition system were employed. The simulated gas system and the catalytic reaction device included eight mass flow controllers to prepare simulated flue gases compositions and a fixed-bed reactor (a quartz tube with an inner diameter of 6 mm and a tube type resistance furnace). The catalyst (40-60 meshes particles) was filled in a quartz tube and fixed with quartz wool. Hg^0 vapor was prepared from the Hg^0 permeation unit and was blended with the gases before they entered the reactor. The concentration of elemental mercury in the gas was analyzed using a mercury analyzer (CVAAS SG-921).

At the beginning of each test, the gas containing the elemental mercury was first passed through the bypass without a catalyst and subsequently sent to the CVAAS to determine the baseline. When the concentration of elemental mercury remained within ± 5% for more than 30 min, the gas was diverted to the fixed-bed reactor with catalysts. 5 ppm HCl was passed to estimate the oxidation efficiency of Hg^0 until the catalysts were saturated. The gas flow rate was 30 L/h, corresponding to a space velocity (SV) of 4.26×10^5 h^{-1}. Nitrogen was used as the carrier gas, and the oxygen content was 4%.

Because the catalysts were first saturated in approximately 300 μg/m^3 Hg^0 plus N_2 and O_2 gas flow, the decrease of Hg^0 concentration across the catalysts after passing HCl was attributed to the Hg^0 oxidation; Besides, the Online Mercury Emissions Monitoring System (3300 RS) proved that Hg^0 in flue gas was oxidized by catalyst;

Furthermore, mercury on the surface of catalysts was analyzed by a RA-915+ mercury analyzer (Lumex, Russia) equipped with a liquid analysis unit and a solid pyrolysis unit (RP-91C), which found the Hg^0 on the surface of catalyst was little, and only a little amount of Hg^{2+} species existed. Accordingly, the definition of Hg^0 oxidation efficiency (Eoxi) over catalysts is as follows:

$$\text{Eoxi}(\%) = \frac{\triangle \text{Hg}^0}{\text{Hg}^0_{\text{in}}} = \frac{\text{Hg}^0_{\text{in}} - \text{Hg}^0_{\text{out}}}{\text{Hg}^0_{\text{in}}}$$

2.4 Characterization of the Catalysts.

The XRD patterns of the catalysts were obtained by an X-ray diffractometer (APLX-DUO, BRUKER, Germany) using Cu Ka radiation (40 kv and 20 mA). The microstructure of the catalysts was analyzed by transmission electron microscopy (TEM). The sample was dispersed in ethanol with strong sonication before the analysis. H_2-TPR experiments were performed on the Chemisorp TPx 2920 instrument, the catalysts were degassed at 200 ℃ for 3 h under Ar at atmosphere before the H_2-TPR test, the reducing gas was 10% H_2/Ar. The X-ray photoelectron spectroscopy (XPS) measurement was conducted using an AXIS UItraDLD (Shimadzu-Kratos) spectrometer with Al Ka as the excitation source. The C1s line at 284.8 ev was taken as a reference for the binding energy calibration. The Cl_2 produced by Deacon Reaction was monitored in situ by a UV/vis spectrometer equipped with an optical fiber for UV-beam transmission and a detector in the range of 200-800 nm. The maximum UV absorbance for chlorine is at approximately 330 nm. The valence state change for mercury was analyzed by the Online Mercury

Emissions Monitoring System (3300 RS). The temperature programmed desorption curves of Hg^0 performed as follows: a known amount of catalysts was placed in the catalytic reaction device with N_2 + 4% O_2 at 30 L/h and 100 ℃ to adsorb mercury for 2 h; afterwards, the oxygen was stopped, and the Hg signal curve was recorded at 2 ℃/min until it reached 450 ℃ under nitrogen.

3. Results and discussion

3.1 The effect of silver on the catalytic oxidation of Hg^0.

Figure 1

Figure 1 shows the comparison of the Hg^0 catalytic oxidation efficiencies over Ce-Ti and Ag-Ce-Ti with various temperatures at 4.26 $\times 10^5$ h^{-1} space velocity. Figure 1 shows that the catalytic efficiency of Ce-Ti and Ag-Ce-Ti were both improved with the increase in temperature. Moreover, the Hg^0 catalytic oxidation efficiency was significantly improved after adding silver whether at a low temperature or at a high temperature, which indicated the silver had an important role in the catalytic performance improvement of the Ce-Ti catalyst. It was also found that Ag-Ce-Ti was an excellent catalyst and had a wide temperature window for oxidizing Hg^0. Therefore, it was necessary to analyze the physical and chemical properties of the catalysts and the reaction mechanism.

3.2 The physical and chemical characterization.

Figure 2

Figure 2 shows the XRD patterns of various catalysts calcined at 500 ℃. The anatase phase and the rutile phase of TiO_2 are clearly seen in Figure 2 (b)-(d). The intensity of the peaks increased after adding silver. This indicates that the catalysts had better crystallization, which was beneficial to the catalysis reaction.[16, 17] The characteristic peaks of CeO_2 were observed in Figure 2 (a), while the peaks were not obvious in Figure 2 (d), which manifested the CeO_2 uniform distribution. Additionally, Ag^0 peaks could be observed in Figure 2 (c) and Figure 2 (d), indicating that metallic silver was present on the support.[18-20]

Figure 3

Figure 3 shows the transmission electron microscopy (TEM) of Ce-Ti and Ag-Ce-Ti. Figure 3 (a) shows that the Ce-Ti catalysts were nanoparticles and the sizes were between 20 and 30 nm. Ceria oxide particles could not be found on the surface of the catalyst, while EDS analysis in Figure 3 (a) could prove the existence of ceria oxide on the carrier, which indicated that ceria atoms were well dispersed on the TiO_2 or the low content referred to the results of XRD. Many small particles were attached on the surfaces of TiO_2, as seen in Figure 3 (b), which were Ag nanoparticles. The size distribution of silver nanoparticles was between 2-3 nm, indicating the silver

nanoparticles were evenly deposited on the titanium.

Figure 4

Figure 4 shows the XPS spectra of Ce-Ti, Ag-Ce-Ti and Ag-Ce-Ti passed 15 ppm HCl at various temperatures. It was reported that the CeO_2 spectrum was composed of two multiplets (v and u), where V and U correspond to the spin-orbit split 3d 5/2 and 3d 3/2 core holes, respectively. The peaks referred to as v, v″ and v ‴ are contributed by CeO_2 and assigned to a mixture of Ce IV ($3d^9 4f^2$) O ($2p^4$), Ce IV($3d^9 4f^1$) O ($2p^5$) and Ce IV ($3d^9$ $4f^0$) O ($2p^6$), respectively. The same peak assignment is applied to u structures. The peaks v_o and v′ are assigned to a mixture of Ce III ($3d^9$ $4f^2$) O ($2p^5$) and Ce III ($3d^9$ $4f^1$) O ($2p^6$), respectively. [9, 21] The Ce 3d spectra collected for the Ag-Ce-Ti was shown in Figure 4 (a). It can be seen that Ce existed in the mixture of Ce (IV) and Ce (III) states, and the characteristic peaks shifted to the high binding energy after adding silver, which indicated that the amount of Ce (IV) states were increased to being beneficial for the oxidation ability. When HCl was passed, the characteristic peaks slightly shifted to the low binding energy, manifesting the decreasing Ce (IV) states, which was because that HCl was oxidized by CeO_2. In addition, the intensity of peaks was not weakened, showing that the HCl was not adsorbed on the CeO_2.

The binding energies of Ag 3d5/2 for Ag, Ag_2O and AgO were 368, 367.7 and 367.4 eV, respectively.[22] The XPS peaks of Ag 3d in Figure 4 (b) clearly show that

silver is mostly present with the metallic state, which indicates that the particles on the TiO_2 are silver nanoparticles referred to the results of TEM. When HCl was passed, the intensity of the characteristic peaks was weakened and shifted to the low binding energy. It may be that the HCl adsorbed on the surface of Ag and Ag^0 was oxidized to Ag^+. The peak of Ag_2O was shifted to the low binding energy, which may be the effect of HCl. With the increasing temperature, the peaks' intensity was enhanced, indicating that the amount of adsorbed Cl was reduced.

The XPS Cl 2p spectra was investigated in this study, shown in Figure 4 (c). Carrasco, et al reported that the Cl 2p spectra were resolved with three spin – orbit split doublets (Cl 2p3/2 and Cl 2p1/2) with the binding energies for the Cl 2p3/2 components at ~ 197, ~ 199 and ~ 200 eV.[23, 24] In Figure 4 (c), the Cl 2p peaks centered at 197.2 and 200.2 eV correspond to ionic (Cl^-) and covalent (– Cl) chlorine species, respectively, whereas the component at 198.3 eV is ascribed to the intermediate chlorine species (Cl*). Figure 4 (c) shows that the chlorine species mainly existed in covalent (– Cl) chlorine species and intermediate chlorine species (Cl*) at 200℃, the covalent (– Cl) chlorine might be the HCl adsorbed on the surface of the catalyst, and the Cl* might be the species that the adsorbed HCl was oxidized. With the increase in temperature, the covalent (– Cl) chlorine was reduced, while the chlorine species (Cl*) and the ionic species (Cl^-) were increased. It indicated that the HCl adsorption ability of the catalyst was poor with the increasing temperature. In addition, the catalyst oxidation ability was enhanced at high temperatures and can improve the yield of Cl*. The appearance of ionic (Cl^-) may be the reduced chlorine

species (Cl*) was, oxidizing the Ce^{3+} and Ag^{0} to Ce^{4+} and Ag^{+}. It can also be found that the peak intensities slowly decreased with increasing temperature, which may be because the adsorbed surface Cl was gradually removed.

The O 1s XPS spectrum is shown in Figure 4 (d). The common main peaks at 529.8 eV might be ascribed to lattice oxygen, and the peak at 531.4 eV could be attributed to surface chemisorbed oxygen. Furthermore, the positions of the O 1s 528.2 eV were nucleophilic states and 530.4 eV denoted electrophilic states, and the electrophilic oxygen could improve the oxidation step of the low valence state to the high valence state for metal ions.[25] Figure 4 (d) shows that there was no nucleophilic oxygen after adding silver, which was beneficial for the oxidation ability of the catalyst. When the HCl was passed at 200 ℃, the characteristic peak of O was shifted, which indicated that surface chemisorbed oxygen had increased. The chemisorbed oxygen was beneficial for the oxidation reaction. With the increase of temperature, the chemisorbed oxygen was reduced, and the adsorption of oxygen on the surface of the catalyst at high temperatures was difficult.

Figure 5

The TPR profiles of the various catalysts are shown in Figure 5. CeO_2 shows three peaks in Figure 5 (a). A peak that appeared at 410 ℃ was corresponded with the reduction of surface oxygen and the peak at approximately 510 ℃ was related to the bulk oxygen,[26] while the peak at approximately 800 ℃ could be assigned to the lattice

oxygen of CeO_2.[27] When CeO_2 was loaded on the TiO_2, the characteristic peak of CeO_2 was shifted to the high temperature, which may have meant that the CeO_2 was dispersed well on the carrier and there was an interaction between the two. A broad reduction peak starting from 100 ℃ and ending at about 180 ℃ could be attributed to the reduction of Ag_2O on the support. [28] The peak for Ag-Ce-Ti that appeared at 120℃ in Figure 5 (d) could be attributed to the reduction of Ag_2O, and the peak that appeared at about 200 ℃ may be related to the reduction of the surface oxygen of CeO_2 referred to Figure 5 (b) and 5 (c),[15, 29] which was indicated by the fact that the peaks of CeO_2 shifted to the low temperature after adding silver. This showed that the redox ability of the catalyst was enhanced and was beneficial for the oxidation reaction.

3.3 The gas component effect analysis.

Figure 6

The gas component effect on the Hg^0 oxidation of Ag-Ce-Ti is shown in Figure 6. The catalytic efficiency was high in the presence of HCl, increasing as the temperature increased. It indicated HCl was the main catalytic component. When SO_2 was added, the Hg^0 oxidation efficiency began to decrease slightly at low temperature, while dropped sharply at high temperature, suggested that Ag-Ce-Ti had a superior resistance toward SO_2 at low temperature, and SO_2 might compete for the active sites to inhibit the reaction of Hg^0 and Cl at high temperature. The Hg^0 oxidation efficiency

improved when adding NO, manifested NO promoted the Hg^0 oxidation. Besides, water inhibited the Hg^0 oxidation both at low temperature and high temperature.

3.4 The catalytic oxidation Hg^0 mechanism analysis.

Figure 7

To clarify the catalytic mechanism of the elemental mercury conversion over Ag-Ce-Ti, the HCl and Hg^0 breakthrough experiments were conducted.

Figure 7 (a) shows the HCl breakthrough curves of Ag-Ce-Ti at various temperatures. Figure 7 (a) shows that HCl could be adsorbed on the surface of Ag-Ce-Ti, either at low temperatures or at high temperatures, and the adsorption ability for HCl was reduced with the increasing temperature. The same trend can be seen from Figure 7 (b), which was shown for the Hg^0 breakthrough curves. The adsorption ability of Hg^0 was a little above 300 ℃, indicating that Hg^0 was hardly adsorbed at high temperatures. It could be concluded that Hg^0 oxidation over Ag-Ce-Ti catalysts probably occurred through adsorbed HCl reacting with adsorbed Hg^0 at low temperatures, the process of which is the Langmuir Hinshelwood mechanism.[9] Furthermore, at high temperatures, Hg^0 oxidation proceeded through the gas-phase or weakly adsorbed Hg^0 reacted with the adsorbed HCl by the Eley Rideal mechanism.[30]

Figure 8

Figure 8 shows Hg^0 breakthrough curves over HCl pretreated Ag-Ce-Ti and Ce-Ti. Figure 8 (a) shows that the catalyst still has oxidation ability when HCl was not passed. This indicates that the chlorine species were adsorbed on the Ag-Ce-Ti and participated in the reaction. The Hg^0 oxidation efficiency had a tendency of increasing first and then reducing slightly with an increase in temperature and was most effective at 300 ℃. Because the catalyst was purged by nitrogen after the HCl was pretreated, there was hardly any Cl_2 adsorbed on the catalyst. The adsorption ability of HCl reduced with the increasing temperature referred to in Figure 7 (a), so that the adsorbed component on the surface of the catalyst for oxidizing Hg^0 could be an active chlorine species formed by the reaction between adsorbed HCl and Ag-Ce-Ti, which could react with Hg^0. The amount of active chlorine species would increase at high temperatures due to the high catalytic ability of Ag-Ce–Ti. However, the amount of adsorbed HCl decreased at high temperatures, so the amount of adsorbed active Cl was highest at 300 ℃, and the Hg^0 oxidation efficiency was the highest. When the temperature was higher than 300 ℃, the Hg^0 oxidation efficiency of Ag-Ce-Ti was low, which indicated that there little active Cl was adsorbed on the surface of catalyst. While the catalytic efficiency of Ag-Ce-Ti was improved with the increasing temperature referred to in Figure 1, it might be because Cl_2 was generated by the reaction of active Cl and further reacted with Hg^0 at high temperature.

Figure 8 (b) shows the Hg^0 breakthrough curves over HCl pretreated Ce-Ti. It shows the same trend as Figure 8 (a). However, the Hg^0 concentration increased with time and was higher than that of Ag-Ce-Ti, which indicated that the adsorbed active

chlorine species was low due to the poor catalytic ability. It revealed that the active chlorine species was mainly adsorbed on silver nanoparticles corresponding to the results of the XPS analysis. Silver was important for the improvement of the catalytic ability.

Figure 9

To verify the role of chlorine, the experiment of Cl_2 produced by Deacon Reaction was carried out. Figure 9 shows the yield of Cl_2 catalyzed by Ag-Ce-Ti after passing 5000 ppm HCl. As can be seen from Figure 9, the characteristic peak of Cl_2 was not found below 400 ℃， indicated that Cl_2 was difficulty to generate at low temperature and chlorine was existed in the form of active Cl. With the increase of temperature, the intensity of Cl_2 characteristic peak started to enhance, manifested the yield of Cl_2 increased, which might be the more gaseous chlorine atoms or the chlorine atoms have higher activity and react with the nearby chlorine atoms on the support at high temperature. The analysis above proved that the active Cl reacted with Hg^0 at low temperature, and active Cl and Cl_2 reacted with Hg^0 at high temperature.

Figure 10

To study the mercury combination property of catalysts, the Hg^0 adsorption and desorption experiment was performed. Figure 10 shows the Hg-TPD curves for

various catalysts after absorption for 2 h. It can be seen form Figure 10 that the adsorption ability for Ce-Ti was poor, which was indicated by the fact that Hg^0 was less adsorbed on the Ce(5%)-Ti in the process of the reaction. For Ag(5%)-Ti, Hg^0 was desorbed as the temperature increased. This may be due to the decomposing of the silver amalgam, indicating that silver was important for adsorbing Hg^0. The mercury combination ability of Ag(5%)-Ce(5%)-Ti was also strong, which is seen in Figure 10. The desorption amount of Hg^0 was similar with that of Ag(5%)–Ti, which manifested that Hg^0 can be absorbed on Ag(5%)-Ce(5%)-Ti at low temperatures, and reacted with the absorbed HCl and active Cl, proving to have an excellent catalytic effect.

Figure 11

Based the results above, the main reaction processes for the Hg^0 oxidation over Ag-Ce-Ti at low temperatures and high temperatures are shown in Figure 11. The active chlorine species and Hg^0 were both adsorbed on silver nanoparticles and reacted with each other at low temperatures following the Langmuir Hinshelwood mechanism. At high temperatures, active chlorine species adsorbed on silver nanoparticles and Cl_2 was reacted with the gas-phase or weakly adsorbed Hg^0 by the Eley Rideal mechanism and the homogeneous gas-phase reaction. It further proved that the Hg^0 oxidation ability could be enhanced by adding silver whether at low temperatures or at high temperatures.

.

Figure 12

Figure 12 shows that the mercury concentration change curves over Ag-Ce-Ti after adding O_2 and HCl at 150 and 350 ℃ as a further proof of the results. Figure 12 shows that the concentration of total mercury and elemental mercury both reduced after O_2 was added either at low temperatures or at high temperatures, and the concentration of elemental mercury was lower than that of total mercury. It indicated that oxygen was important for the Hg^0 oxidation. In addition, a greater amount of Hg^{2+} was generated at high temperatures than at low temperatures, showing that the oxidation ability of Ag-Ce-Ti was higher at high temperatures under oxygen conditions. When HCl was added, the concentration of elemental mercury was further reduced at both 150 ℃ and 350 ℃, and the gap between Hg^0 and Hg^t was larger, which indicated that HCl was the major catalytic component. The decreasing concentration of Hg^0 was such that Hg^0 reacted with the adsorbed active Cl species and chlorine to produce $HgCl_2$. The concentration of total mercury was also reduced, which may have caused a small amount of $HgCl_2$ to be adsorbed onto the catalyst.

4. Conclusions

The silver-doped Ce-Ti catalyst can significantly improve the performance of the catalyst at various temperatures. The characterization results indicated that silver nanoparticles were deposited on the titanium and the catalysts had better

crystallization after adding silver. The silver existed mostly in its metallic state. The silver can keep the element of Ce in a greater amount of Ce(IV) states, and HCl was oxidized to active Cl by CeO_2 and then was adsorbed on the silver nanoparticles. The gas component analysis indicated that SO_2 and water inhibited slightly the Hg^0 oxidization, and NO can promote the reaction. HCl and Hg^0 breakthrough curves and Cl_2 yield experiment revealed that active chlorine species and Hg^0 were both adsorbed on silver nanoparticles and reacted with each other at low temperatures following the Langmuir Hinshelwood mechanism. At high temperatures, active chlorine species adsorbed on silver nanoparticles and chlorine were reacted with the gas-phase or weakly adsorbed Hg^0 by the Eley Rideal mechanism and the homogeneous gas-phase reaction. These results proved that the Hg^0 oxidation ability could be enhanced by adding silver whether at low temperatures or at high temperatures. Furthermore, the Hg^0 adsorption and desorption experiment showed that the mercury combination ability of Ce(5%)-Ti was enhanced by adding silver. Finally, the valence state change for mercury was analyzed to indicate that HCl was the major catalytic oxidization component.

Acknowledgments

This study was supported by the Major State Basic Research Development Program of China (973 Program, No. 2013CB430005), the National Natural Science Foundation of China (No. 50908145) and the National High-Tech R&D Program (863) of China (No. 2011AA060801).

References

1. H. Yang, W. Hou, H. Zhang and L. Zhou, *International Journal of Environmental Science and Technology*, 2013, 10, 689-696.
2. .
3. J. Dong, Z. H. Xu and S. M. Kuznicki, *Environmental Science & Technology*, 2009, 43, 3266-3271.
4. Y. Li, M. Daukoru, A. Suriyawong and P. Biswas, *Energy & Fuels*, 2009, 23, 236-243.
5. N. Q. Yan, W. M. Chen, J. Chen, Z. Qu, Y. F. Guo, S. J. Yang and J. P. Jia, *Environmental Science & Technology*, 2011, 45, 5725-5730.
6. Y. Liu, Y. J. Wang, H. Q. Wang and Z. B. Wu, *Catalysis Communications*, 2011, 12, 1291-1294.
7. J. F. Li, N. Q. Yan, Z. Qu, S. H. Qiao, S. J. Yang, Y. F. Guo, P. Liu and J. P. Jia, *Environmental Science & Technology*, 2010, 44, 426-431.
8. W. J. Lee and G. N. Bae, *Environmental Science & Technology*, 2009, 43, 1522-1527.
9. H. Li, C.-Y. Wu, Y. Li and J. Zhang, *Environmental science & technology*, 2011, 45, 7394-7400.
10. H. L. Li, C. Y. Wu, L. Q. Li, Y. Li, Y. C. Zhao and J. Y. Zhang, *Fuel*, 2013, 113, 726-732.
11. C. W. Lee, S. D. Serre, Y. Zhao, S. J. Lee and T. W. Hastings, *Journal of the Air & Waste Management Association*, 2008, 58, 484-493.
12. T. Kou, D. Li, C. Zhang, Z. Zhang and H. Yang, *Journal of Molecular Catalysis A: Chemical*, 2014, 382, 55-63.
13. X. Yang, F. Ma, K. Li, Y. Guo, J. Hu, W. Li, M. Huo and Y. Guo, *Journal of hazardous materials*, 2010, 175, 429-438.
14. R. Delaigle, P. Eloy and E. M. Gaigneaux, *Catalysis Today*, 2011, 175, 177-182.
15. L. Ma, D. Wang, J. Li, B. Bai, L. Fu and Y. Li, *Applied Catalysis B-Environmental*, 2014, 148, 36-43.
16. B. M. Reddy, A. Khan, P. Lakshmanan, M. Aouine, S. Loridant and J.-C. Volta, *The Journal of Physical Chemistry B*, 2005, 109, 3355-3363.
17. H. Li, J. Li and Y. Huo, *The Journal of Physical Chemistry B*, 2006, 110, 1559-1565.
18. B. Xin, L. Jing, Z. Ren, B. Wang and H. Fu, *The Journal of Physical Chemistry B*, 2005, 109, 2805-2809.
19. M. Wen, L. Zhou, W. Guan, Y. Li and J. Zhang, *Applied surface science*, 2010, 256, 4226-4230.
20. C. Hu, Y. Lan, J. Qu, X. Hu and A. Wang, *The Journal of Physical Chemistry B*, 2006, 110, 4066-4072.
21. E. Beche, P. Charvin, D. Perarnau, S. Abanades and G. Flamant, *Surface and Interface Analysis*, 2008, 40, 264-267.
22. S. B. Atla, C.-C. Chen, C.-Y. Chen, P.-Y. Lin, W. Pan, K.-C. Cheng, Y. M. Huang, Y.-F. Chang and J.-S. Jean, *Journal of Photochemistry and Photobiology a-Chemistry*, 2012, 236, 1-8.
23. P. M. Carrasco, M. Cortazar, E. Ochoteco, E. Calahorra and J. A. Pomposo, *Surface and Interface Analysis*, 2007, 39, 26-32.
24. H. Piao, K. Adib and M. A. Barteau, *Surface Science*, 2004, 557, 13-20.

25. V. V. Kaichev, V. I. Bukhtiyarov, M. Havecker, A. Knop-Gercke, R. W. Mayer and R. Schlogl, *Kinetics and Catalysis*, 2003, 44, 432-440.
26. S. Watanabe, X. L. Ma and C. S. Song, *Journal of Physical Chemistry C*, 2009, 113, 14249-14257.
27. P. Li, Y. Xin, Q. Li, Z. P. Wang, Z. L. Zhang and L. R. Zheng, *Environmental Science & Technology*, 2012, 46, 9600-9605.
28. S. Zhao, Y. Ma, Z. Qu, N. Yan, Z. Li, J. Xie and W. Chen, *Catalysis Science & Technology*, 2014, Advance Article.
29. Y. Kang, M. Sun and A. Li, *Catalysis letters*, 2012, 142, 1498-1504.
30. W. Gao, Q. C. Liu, C. Y. Wu, H. L. Li, Y. Li, J. Yang and G. F. Wu, *Chemical Engineering Journal*, 2013, 220, 53-60.

Figure Captions

Figure 1 The comparison of the Hg^0 catalytic oxidation efficiencies over Ce-Ti and Ag-Ce-Ti with various temperatures at $4.26*10^5$ h^{-1} space velocity.

Figure 2 The XRD patterns of various catalysts calcined at 500 ℃: CeO_2 (a), Ce(5%)-Ti (b), Ag(5%)-Ti (c) and Ag(5%)-Ce(5%)-Ti (d).

Figure 3 The transmission electron microscopy (TEM) of Ce-Ti and Ag-Ce-Ti: Ce-Ti (a) and Ag-Ce-Ti (b).

Figure 4 The XPS spectra of Ce-Ti, Ag-Ce-Ti and Ag-Ce-Ti passed 15 ppm HCl at various temperatures: Ce 3d (a), Ag 3d (b), Cl 2p (c) and O 1s (d).

Figure 5 The TPR profiles of the various catalysts: CeO_2 (a), Ce-Ti (b) and Ag-Ce-Ti (c).

Figure 6 The gas component effect on the Hg^0 oxidation of Ag-Ce-Ti.

Figure 7 The HCl and Hg^0 breakthrough curves of Ag-Ce-Ti at various temperatures: HCl breakthrough curves (a) and Hg^0 breakthrough curves (b).

Figure 8 Hg^0 breakthrough curves over HCl pretreated Ag-Ce-Ti and Ce-Ti: Ag-Ce-Ti (a) and Ce-Ti (b).

Figure 9 The yield of Cl_2 catalyzed by Ag-Ce-Ti after passing 5000 ppm HCl.

Figure 10 The Hg-TPD curves for various catalysts.

Figure 11 The reaction process for the Hg^0 oxidation over Ag-Ce-Ti at low temperatures and high temperatures.

Figure 12 The mercury concentration change curves over Ag-Ce-Ti after adding O_2 and HCl at 150 ℃ and 350 ℃: 150 ℃ (a) and 350 ℃ (b).

476 **Figure 1**

477

478

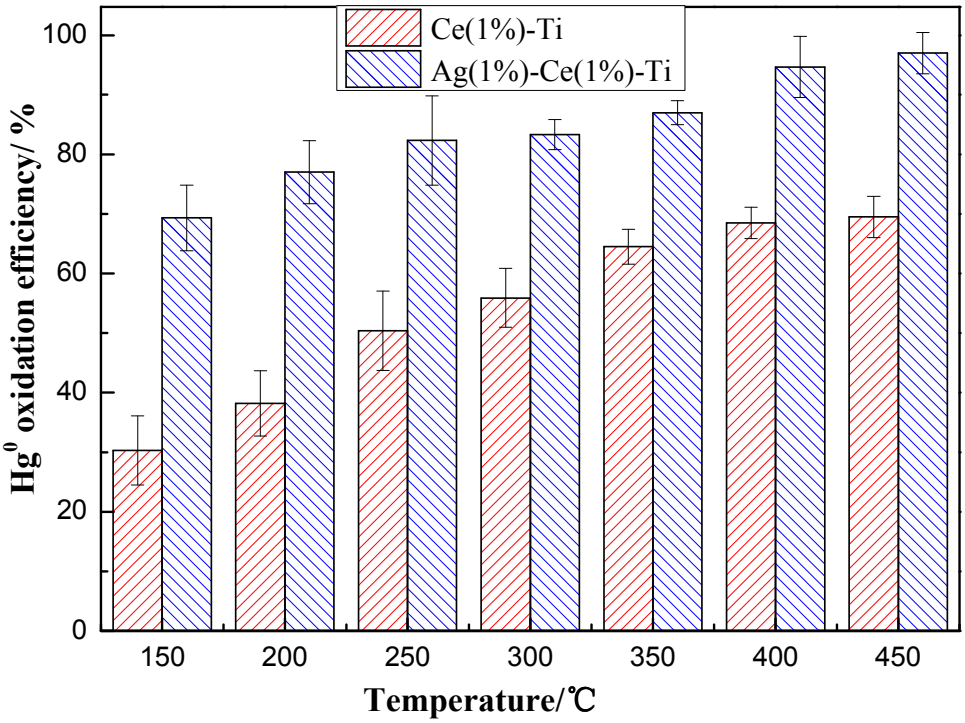

479

480

481 **Figure 2**

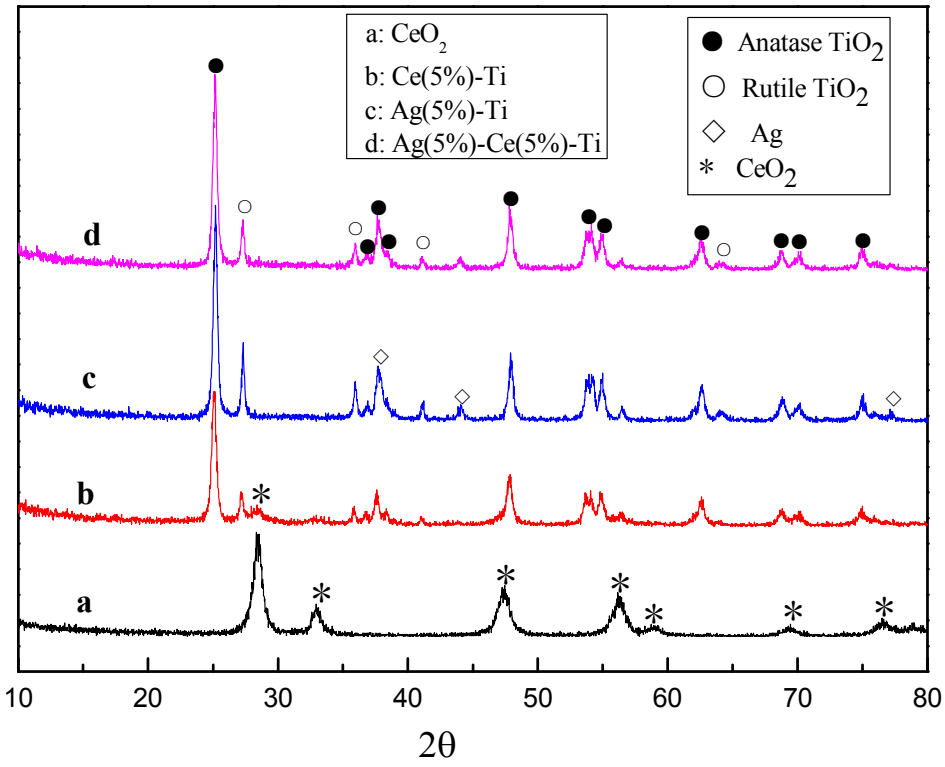

482

483

484

485 **Figure 3**

486

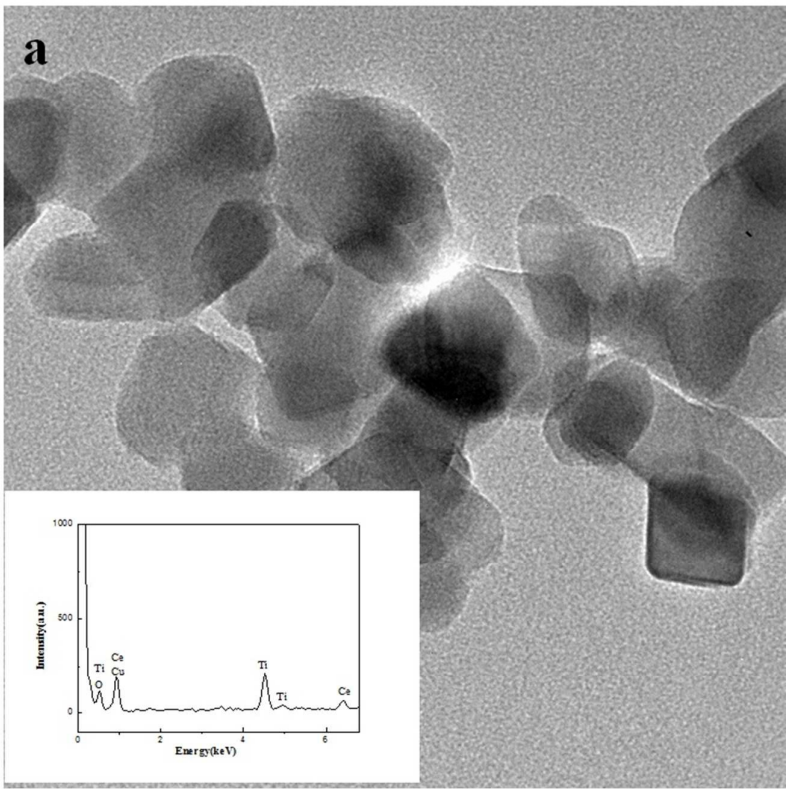

487

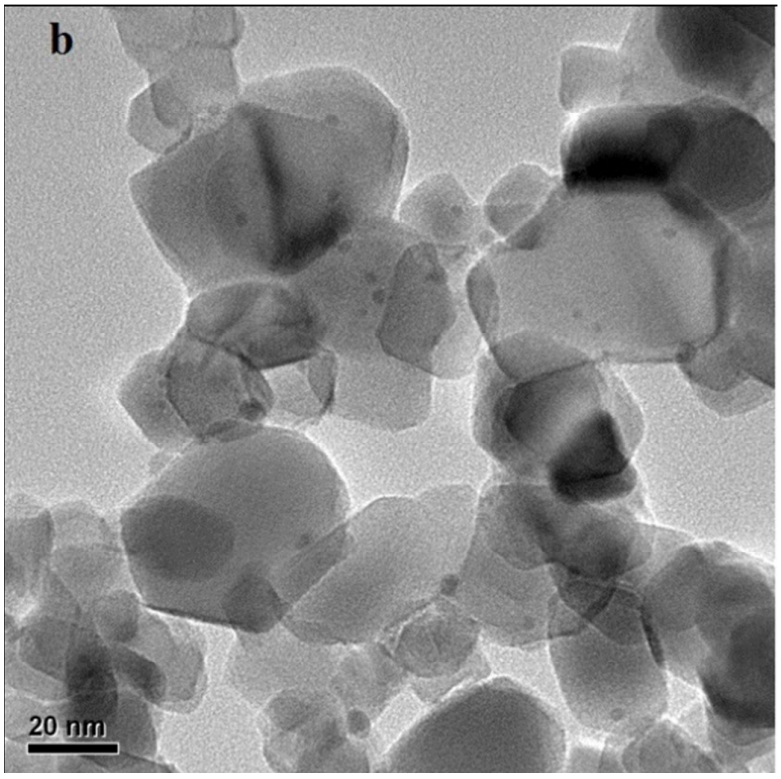

488

494 **Figure 4**

495

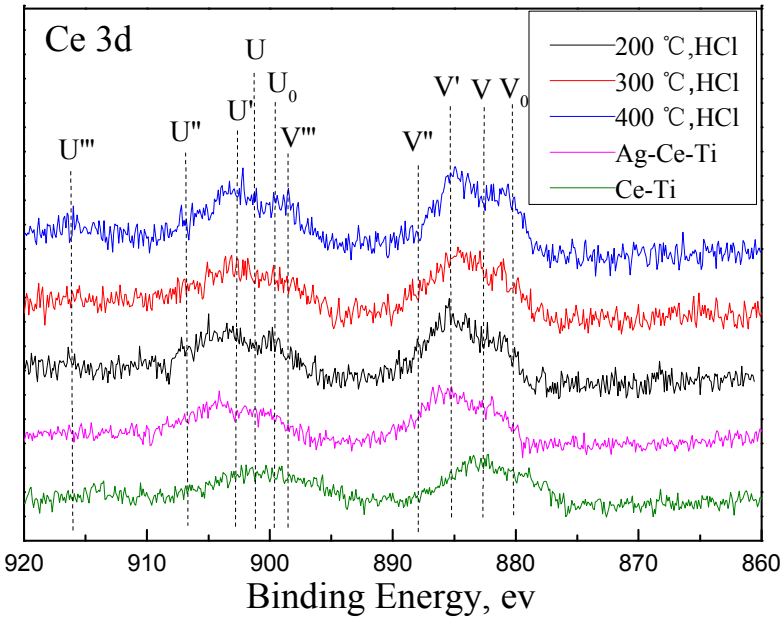

a

496

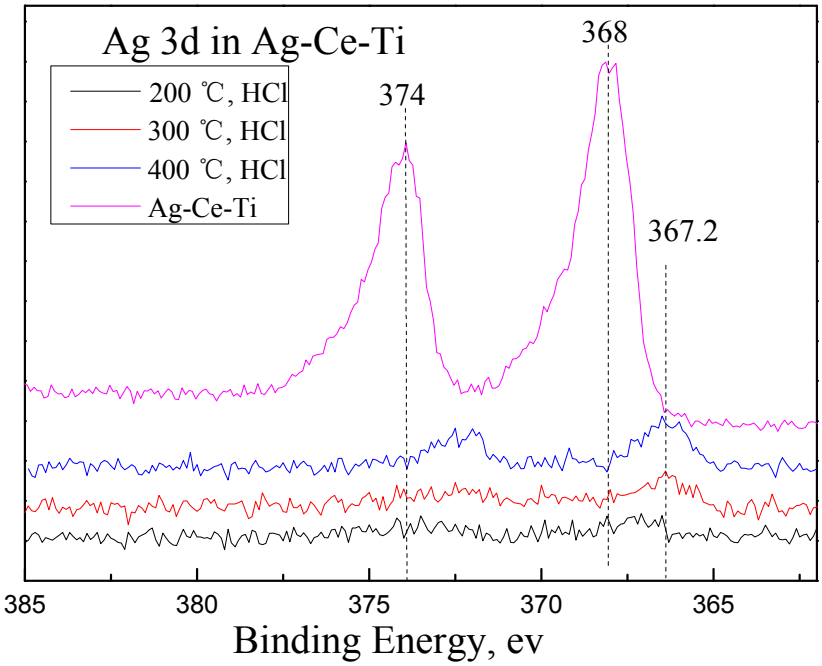

b

497

498

499

500 **Figure 4**

501

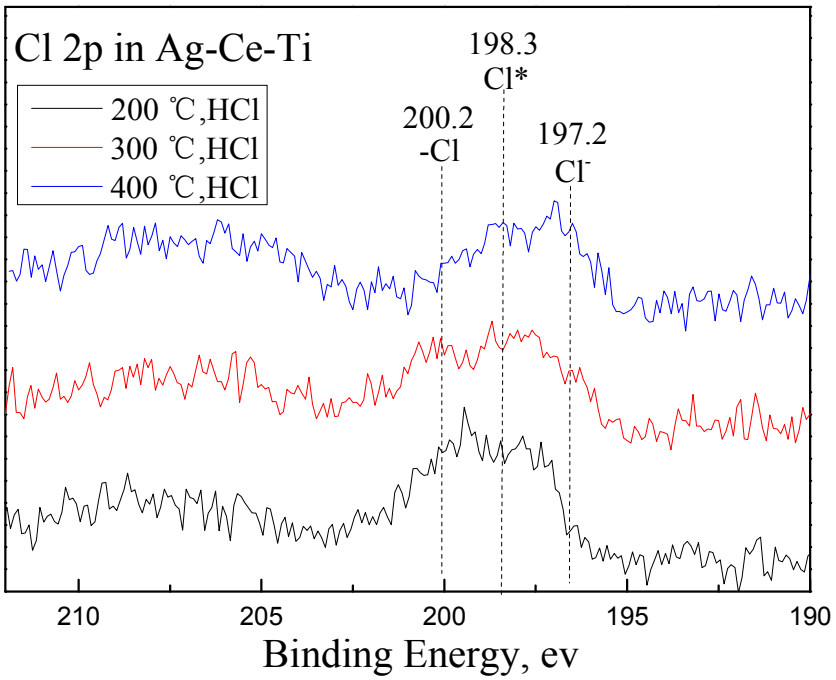

c

502

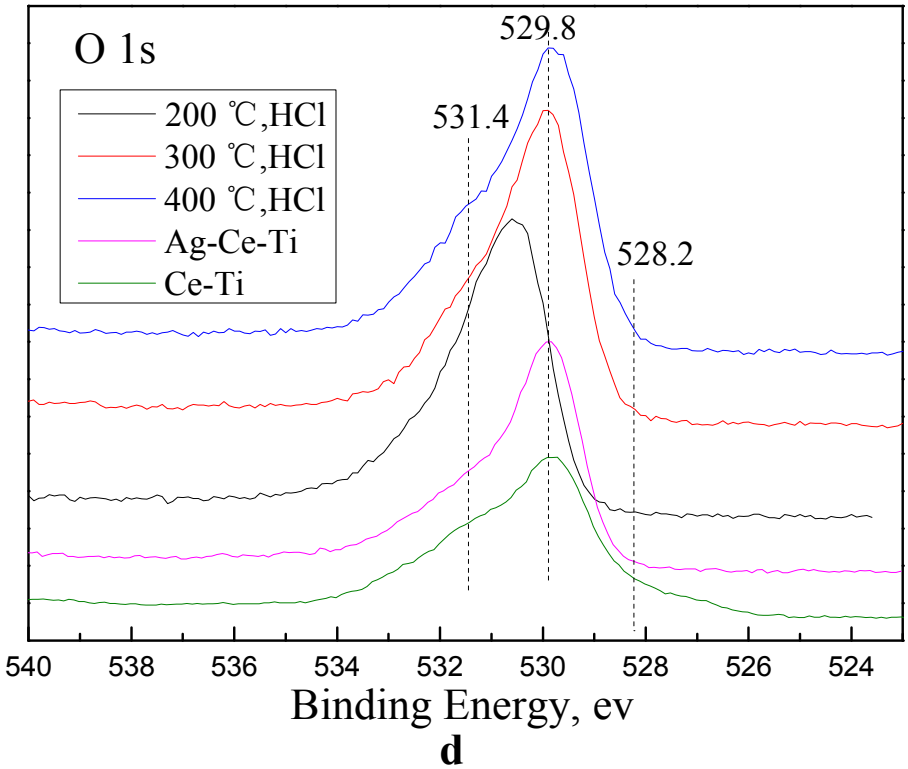

d

503

504 **Figure 5**

505

506

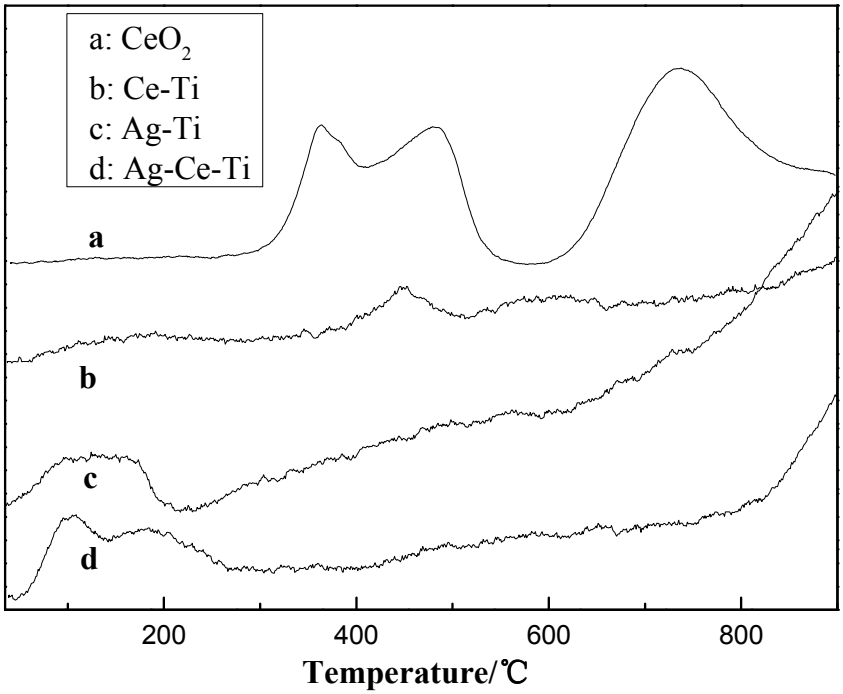

507

508

509 **Figure 6**

510

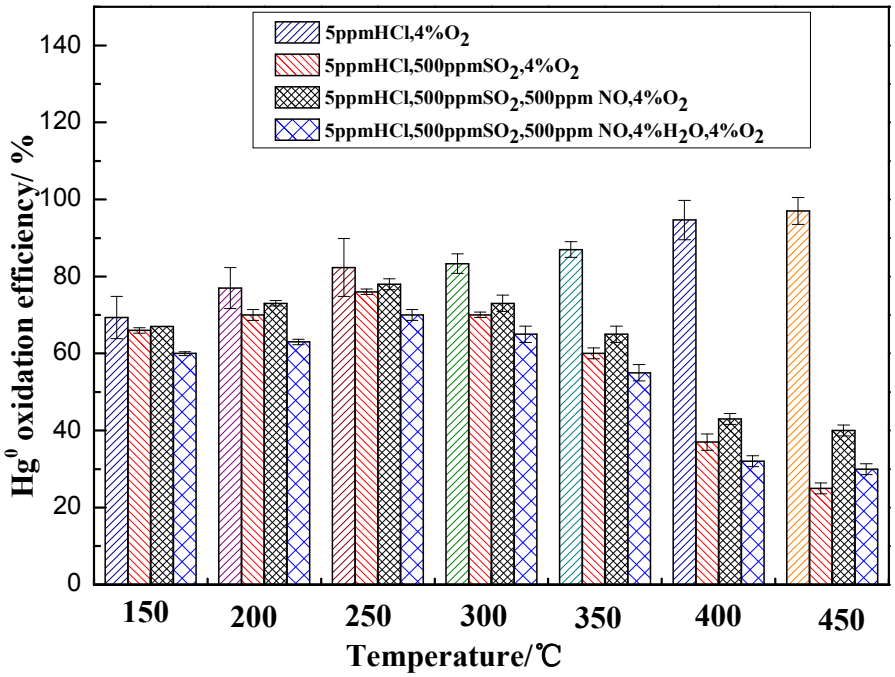

511

512

513

514

515

516

517

518

519

520

521

522

523

524

525

526 **Figure 7**

527

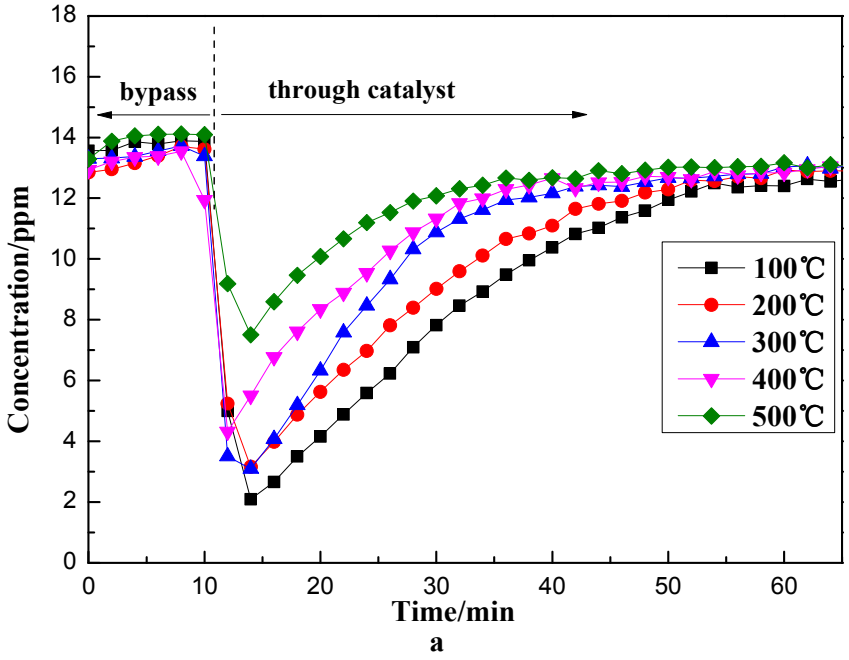

a

528

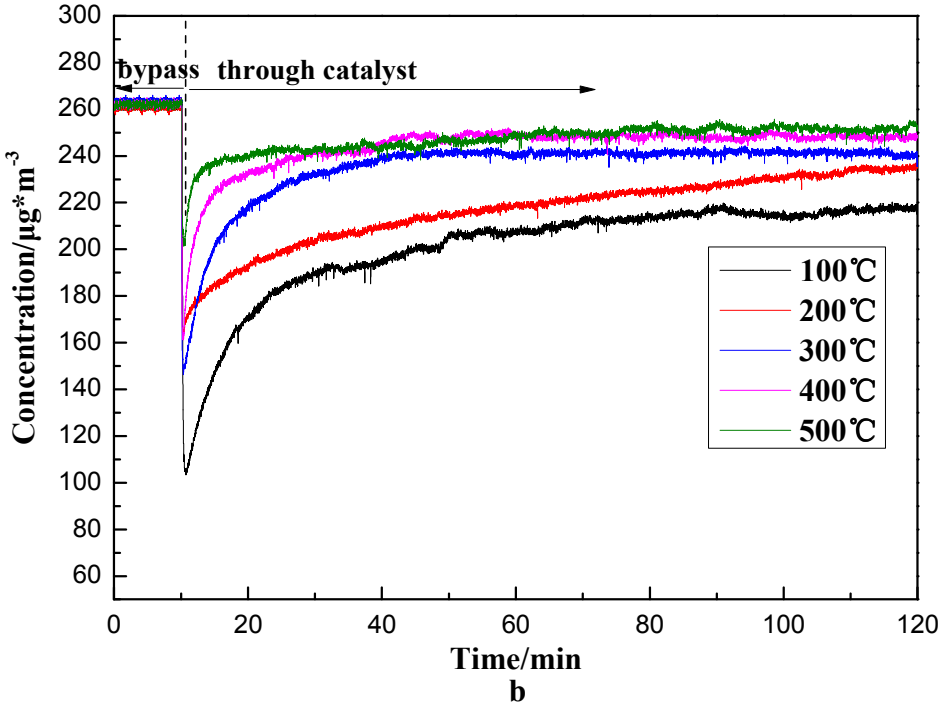

b

529

530

531 **Figure 8**

532

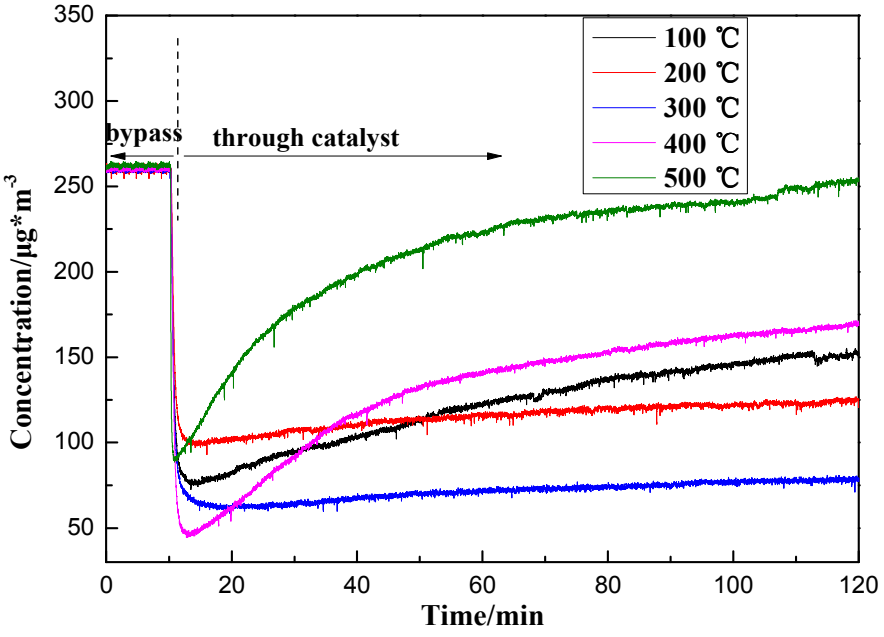

533 **a**

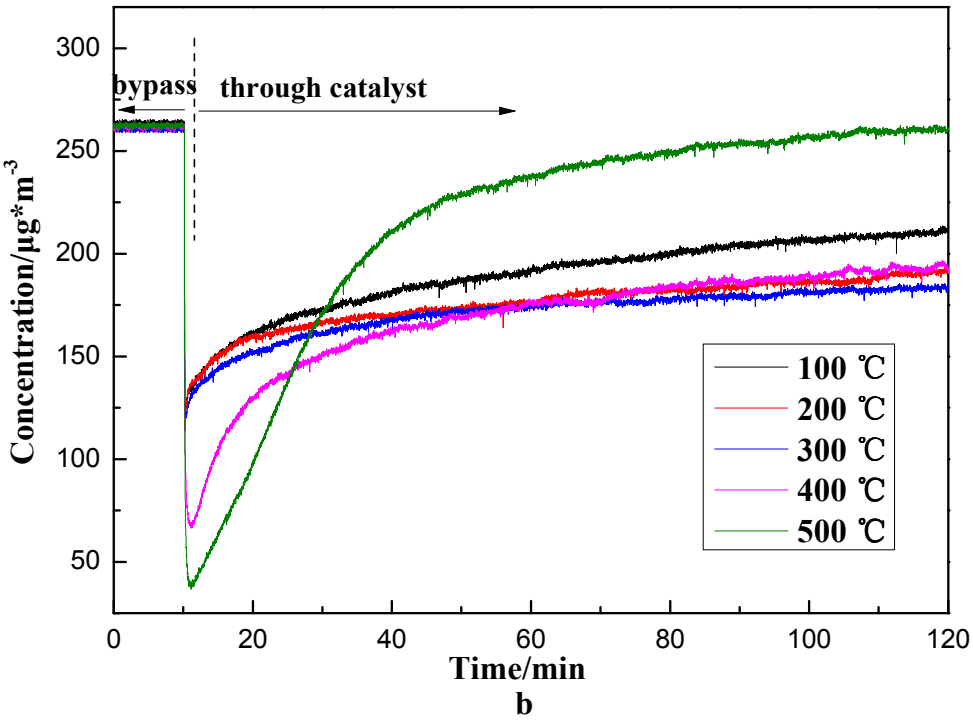

534 **b**

535

536

537 **Figure 9**

538

539

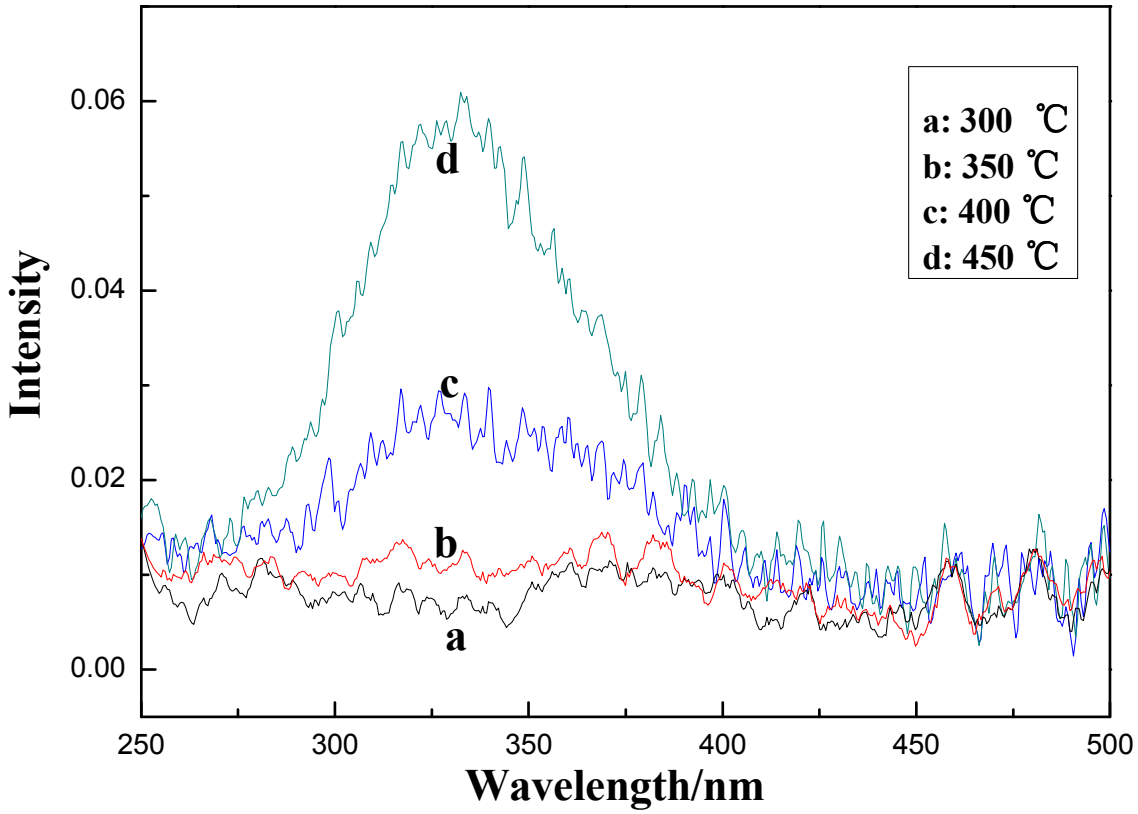

540

541

542 **Figure 10**

543

544

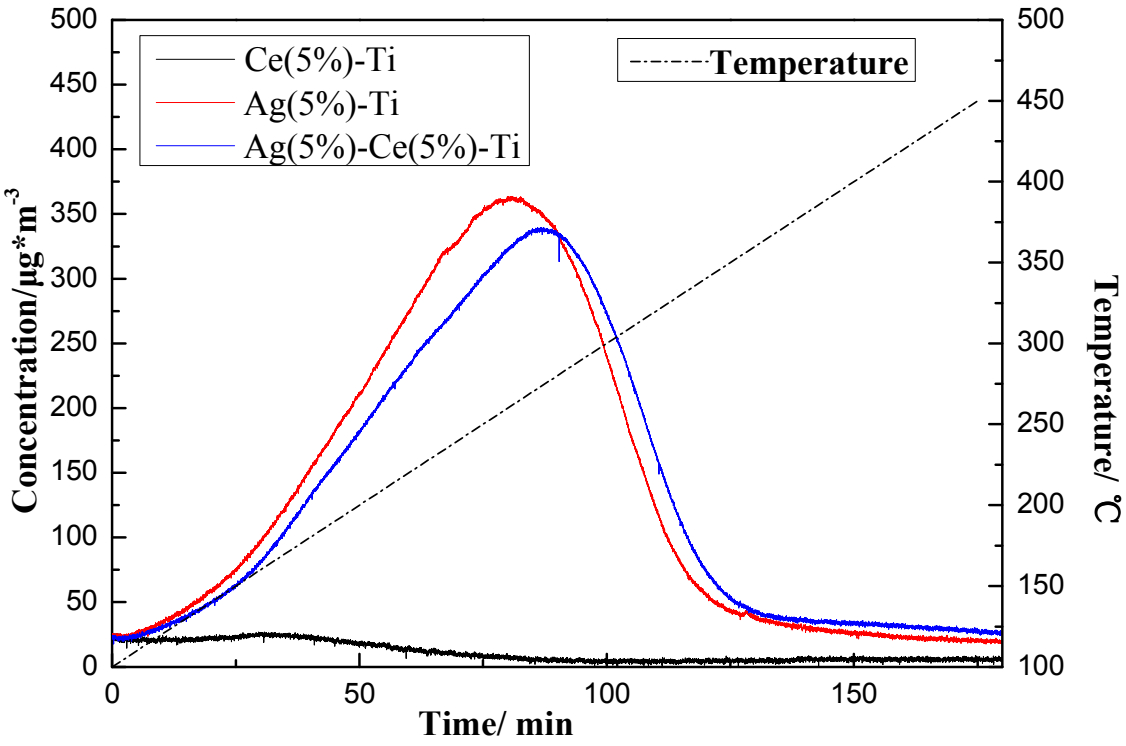

545

546

547 **Figure 11**

548

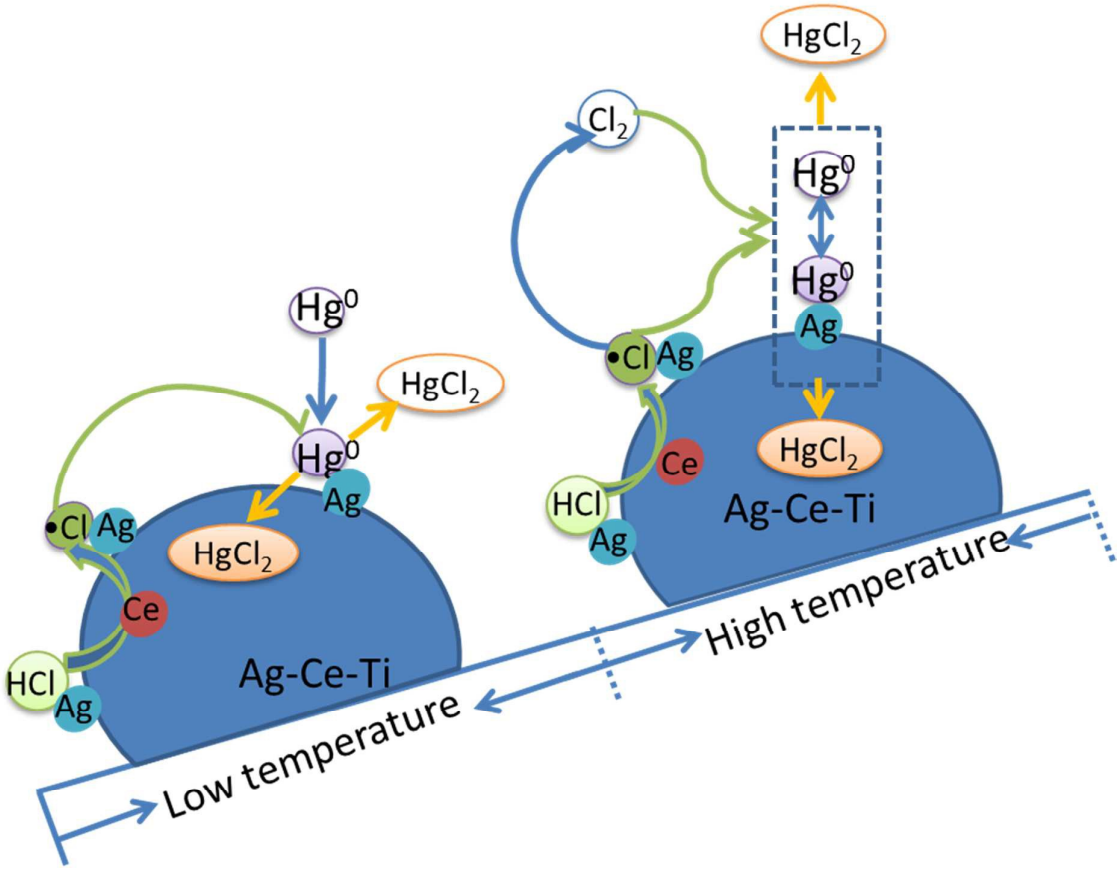

549

550

551 **Figure 12**

552

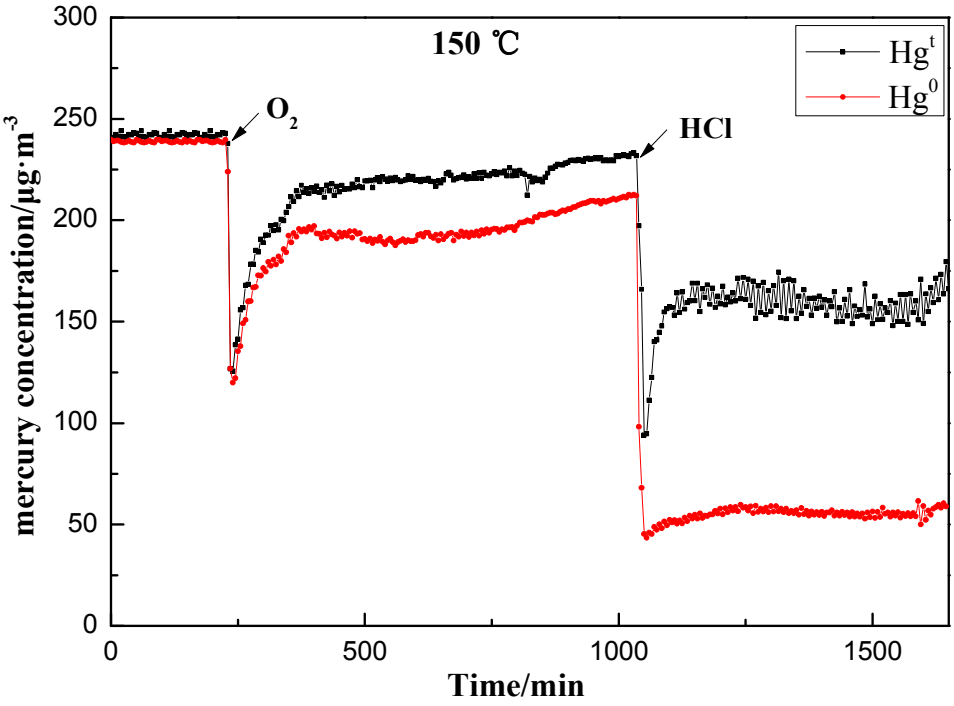

553 **a**

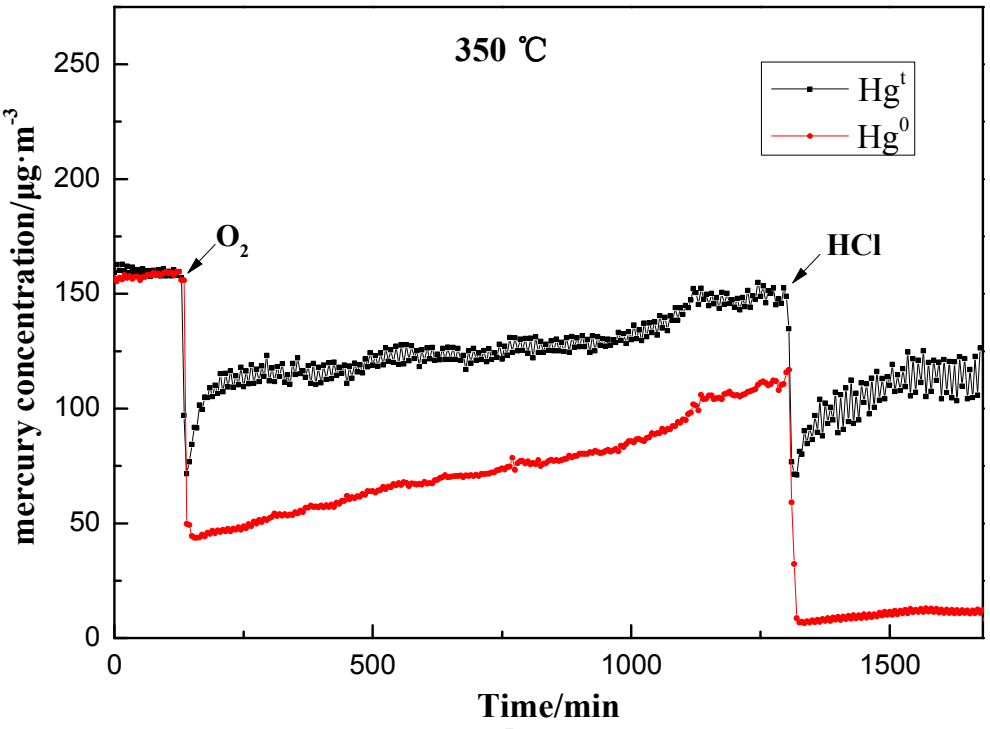

554 **b**

555